Geomorphology 332 (2019) 122–137

Contents lists available at ScienceDirect

Geomorphology

journal homepage: www.elsevier.com/locate/geomorph

Predicting macroturbulence energy and timescales for flow over a gravel bed: Experimental results and scaling laws

Amirreza Ghesemi [a,b], Jimmy Fox [c,*], Admin Husic [d]

[a] Department of Civil, Environmental, and Geo-Engineering, University of Minnesota, Minneapolis, MN, USA
[b] St. Anthony Falls Laboratory, University of Minnesota, Minneapolis, MN, USA
[c] Department of Civil Engineering, University of Kentucky, Lexington, KY, USA
[d] Department of Civil, Environmental, and Architectural Engineering, University of Kansas, Lawrence, KS, USA

ARTICLE INFO

Article history:
Received 1 October 2018
Received in revised form 5 February 2019
Accepted 6 February 2019
Available online 15 February 2019

Keywords:
Macroturbulence
Gravel bed river
Sediment transport applications
Measurement length

ABSTRACT

The fluvial science community lacks predictive equations for macroturbulence energy and timescales, which may serve useful for predicting sediment transport in rivers. Therefore, we investigated the systematic variation of macroturbulence scales by varying hydraulic parameters in an experimental facility, collecting velocimetry data and measuring macroturbulence scales with spectral analyses, and testing scaling laws for macroturbulence prediction that consider inner variables, outer variables, and turbulence kinetic energy. Experiments spanned across 11 energy gradients and aspect ratio combinations including 116 testing conditions each with 30 minute instantaneous turbulence time-series collected. Results showed velocimetry data and time-average turbulence parameters supported the presence of an equilibrium outer region and coherent double-layer assumed in the experimental design. Macroturbulence and bursting wavenumbers were constant in the outer region when scaled with the flow depth, and were independent of distance above the boundary, aspect ratio, energy gradient, Froude number, or Shields parameter. Data results agreed with the derivation herein and showed macroturbulence energy scales with the streamwise turbulence kinetic energy. Semi-theoretical equations for turbulence kinetic energy scaled macroturbulence energy reasonably well. A novel equation is presented for the macroturbulence period, and the equation's transferability is supported by consistency with past macroturbulence studies, bursting formula, and flow visualization studies. Novel equations are presented for macroturbulence energy, and transferability is supported on theoretical and empirical grounds; however open questions remain regarding a universal function for streamwise turbulence kinetic energy and the net contribution of macroturbulence to total turbulence energy. Results showed the macroturbulence wavenumber required a relatively long duration of data (i.e., 17 min) to stabilize. Results were used to formulate a time scale for minimum measurement length of turbulence data when information about macroturbulence is sought after. We discuss macroturbulence linkages with sediment transport, including, prediction of the sediment carrying capacity via macroturbulence formula as one application to help close the gap between turbulence and fluvial sediment transport.

1. Introduction

Prediction of the energy and timescales of macroturbulence has the potential to improve our understanding of flow and sediment interactions in rivers. Our motivation was to predict the energy and timescales of macroturbulence using scaling laws for open channel flow over a gravel bed. Turbulence energy production in open channel flow is believed to occur via the coherent double-layer, which includes bursting associated with near-bed shedding and macroturbulence associated with large-scale alternating momentum zones (Matthes, 1947; Nezu and Nakagawa, 1993; Shvidchenko and Pender, 2001; Roy et al., 2004; Fox et al., 2005; Marquis and Roy, 2006; Hurther et al., 2007; Belcher and Fox, 2009; MacMahan et al., 2012; Stewart and Fox, 2015). Macroturbulence redistributes fluid momentum across the full flow depth, elongates many times the flow depth in the streamwise direction, and is believed to interact with near bed bursting (Roy et al., 2004). Based on this previous work, we expect macroturbulence energy to control organization of turbulence energy in the outer region of river flows. Macroturbulence timescales reflect the period of the phenomena, which shows analogy to timescales of other turbulence structures (e.g., Luchik and Tiederman, 1987; Eder et al., 2015). Prediction of timescales and energy is useful for mass transfer prediction.

The presence of macro-sized eddies has become ubiquitous in a range of turbulent flows and is described with community-specific taxonomy, such as large scale coherent structures in atmospheric

* Corresponding author.
E-mail address: james.fox@uky.edu (J. Fox).

https://doi.org/10.1016/j.geomorph.2019.02.006
0169-555X/

List of symbols

B	flume width
B/H	aspect ratio
D_{84}	particle diameter for which 84% of particles are finer
Fr	$U(gH)^{-1/2}$ is the Froude number
H	flow depth
H/k_s	relative submergence
K	wavenumber
K_b	bursting wavenumber
K_m	macroturbulence wavenumber
$RMS(u')$	root mean square of streamwise velocity fluctuation
$RMS(v')$	root mean square of vertical velocity fluctuation
$RMS(w')$	root mean square of transverse velocity fluctuation
$Rey(u'v')$	shear Reynolds stress
S	spectral energy density
S_b	bursting spectral energy density
S_e	energy gradient
S_m	macroturbulence spectral energy density
SPE	spectral production energy
T_b	busting period
T_m	macroturbulence period
U	time-averaged streamwise velocity
U_0	appropriate velocity scale
U_{max}	maximum streamwise velocity
V	time-averaged vertical velocity component
W	time-averaged transverse velocity component
c_m	empirical constant
f	frequency
g	gravitational acceleration
k_s	roughness height
l	indicate length scale
u	instantaneous streamwise velocity
u'	instantaneous streamwise velocity fluctuation
u_*	friction velocity
v	instantaneous wall normal velocity
v'	instantaneous wall normal velocity fluctuation
w	instantaneous transverse velocity
w'	instantaneous transverse velocity fluctuation
y	wall normal distance above flume bed
σ^2	spectral signal variance
τ	fluid shear stress
ν	kinematic viscosity

turbulence, very large scale motions in pipeflow, superstructures in zero-pressure gradient boundary layers, and macroturbulence in gravel bed rivers (Shvidchenko and Pender, 2001; Guala et al., 2006; Hutchins and Marusic, 2007; Calaf et al., 2013). However, the scaling of macro-sized coherency and its interaction with near-bed shedding is not ubiquitous and rather shows dependence on the type of boundary layer (e.g., pipeflow, channel flow, zero-pressure) and the Reynolds number (Monty et al., 2009; Guala et al., 2011). The fluvial science community currently lacks predictive equations for macroturbulence energy and timescales for open channel flow over gravel beds, and we feel predictive equations may be useful for coupling flow with suspended sediment transport in rivers. For this reason, we measure and scale macroturbulence over a hydraulically rough gravel bed with a logarithmic or log-wake outer region.

We adopt the spectral approach to investigate macroturbulence in open channel flow over a gravel bed. The spectrum of the velocity signal is useful for identifying prominent coherent scales bounding the spectral production region (i.e., the negative one spectral power region, Perry and Abell, 1975; Kim and Adrian, 1999; Calaf et al., 2013). Very large scale coherency (i.e., macroturbulence) is manifested as a broad peak in the streamwise velocity spectra at the low wavenumber boundary of the spectral production region while smaller scale coherency (i.e., bursting) is manifested as the high wavenumber boundary of the region (Kim and Adrian, 1999; Fox et al., 2005; MacMahan et al., 2012; Calaf et al., 2013; Stewart and Fox, 2015). This concept has been shown using theoretical grounds and empirical evidence (Perry and Chong, 1982; Perry et al., 1986; Kim and Adrian, 1999; Calaf et al., 2013).

Gravel bed river studies have highlighted the macroturbulence imprint upon the streamwise velocity spectra (MacMahan et al., 2012; Stewart and Fox, 2015), however we find the spectral approach is underutilized for investigating macroturbulence scales in open channel flow over gravel beds. Few, if any, gravel bed studies have investigated the systematic variation of macroturbulence scales by varying hydraulic parameters in the laboratory and measuring macroturbulence scales with spectra. A number of reasons contribute to this lack of previous work. First is the fairly recent acceptance of macroturbulence as part of the double-layer for open channel flow over gravel beds (Roy et al., 2004; Hurther et al., 2007; Stewart and Fox, 2015). Second, a deterrent for using the spectral production region has been ambiguity surrounding the wavenumber boundaries (i.e., macroturbulence and bursting). For example, smoothing operations (i.e., low pass filters) often coupled with spectral analysis have the potential to shift spectral bounds. Third, reporting of the sensitivity of spectral boundaries to velocimetry methods is lacking. For example, few gravel bed river studies have investigated the stationarity of spectra as a function of data collection duration.

In this paper, we measure systematic variation of macroturbulence periodicity and energy for open channel flow over a gravel bed, and we then consider two commonly held turbulence hypotheses to predict macroturbulence via scaling laws. The first turbulence hypothesis assumed is the aforementioned coherent double-layer. The second hypothesis considered is the equilibrium assumption for the outer region of turbulent open channel flow over a gravel bed. The equilibrium assumption suggests the outer region has balanced turbulence energy generation and dissipation and shows constant dependence on a velocity scale and turbulence length scales (Clauser, 1954, 1956; Townsend, 1976; Nezu and Nakagawa, 1993; George and Castillo, 1997). Regarding scale dependence, the most widely cited velocity scale for prediction is the friction velocity derived by Clauser's (1954, 1956) equilibrium definition although the freestream velocity derived by George and Castillo's (1997) equilibrium definition has gained popularity in recent years. The constant turbulence length scales in outer region equilibrium has been much more ambiguous (e.g., inner, outer and mixed scales), but we expect the characteristic lengths of the turbulence double-layer to conform to the equilibrium definition. We test scaling macroturbulence periodicity and energy with velocity and length scales in this paper.

Our objectives were to (i) collect velocimetry data and calculate time-average turbulence parameters for a range of open channel flows over a gravel bed, (ii) measure macroturbulence and bursting time and energy scales via the spectral approach, and (iii) scale macroturbulence and bursting wavenumbers and energy that lead to predictive equations. The objectives provide the structural subheadings of the methods and results sections. We then discuss implications and transferability of novel predictive equations for macroturbulence in the discussion section. Specifically, we discuss macroturbulence linkages with sediment transport, including, prediction of the sediment carrying capacity via macroturbulence formula as one application to help close the gap between turbulence and fluvial sediment transport.

2. Experimental design

We designed experiments to consider macroturbulence response variables and thereafter the response variables were investigated against dimensionless numbers derived from hydraulic principles. The response variables are defined as the spectral scales of macroturbulence, including its wavenumber (K_m) and energy (K_mS_m).

The spectral scales of bursting (K_b, K_bS_b) are also estimated and reported, although their emphasis is as a comparison to macroturbulence scales and to show consistency of our study with previously reported results of open channel bursting.

The premise for the experimental design was that the response variables could be identified using the velocity spectra (Fig. 1) whereby macroturbulence and bursting wavenumbers (K_m and K_b) bound the spectral production region (Perry et al., 1986; Kim and Adrian, 1999; Stewart and Fox, 2015). Identification of the boundary wavenumbers is possible given the nearly constant energy of the spectral production region (Katul and Chu, 1998). The spectral production region is shown to have a constant negative one slope when plotted as streamwise spectral energy density (see Fig. 1b). Spectral density is plotted on a log-log scale with power spectral density in the vertical axis and wavenumber on the horizontal axis. In order to gain more information about the energy or variance that an individual wavenumber exhibits, the spectra can be plotted in a variance preserving form (Boppe and Neu, 1995; Kim and Adrian, 1999; Venditti and Bennett, 2000). The variance preserving form, also called the pre-multiplied spectra, is a semi-log spectral plot in which the vertical axis is the product of the power spectral density and its corresponding wavenumber (i.e., the spectral energy) while the log-scale horizontal axis is the wavenumber. This type of plot is called 'variance preserving' since the area under the curve between two wavenumbers corresponds to the spectral signal variance (σ^2), which is also the streamwise turbulence energy, in the specified interval. The plotting preserves the turbulence energy mathematically as

$$\sigma^2 = \int_{k_1}^{k_2} KS(K)\mathrm{d}(\log(K)) = \int_{k_1}^{k_2} S(K)dK \tag{1}$$

where K is wavenumber and $S(K)$ is spectral energy. The variance preserving form plot in Fig. 1 shows that the negative one slope of the spectral density plot is a region in which all eddy scales have the same energy associated with them. This idea can also be shown by calculating the constant negative one slope of the spectral production region using its lower bound (K_m, S_m) and upper bound (K_b, S_b). The result is the constant energy of macroturbulence and bursting scales as.

$$K_mS_m(K_m) = K_bS_b(K_b). \tag{2}$$

Using these principles, the response variables (K_m and K_mS_m) can be identified with the spectral plots for different hydraulic conditions.

Our intent was to investigate macroturbulence response variables within flow over gravel for a wide range of hydraulic conditions. However, as will be shown, a number of variables were fixed in order to limit our experimental design to a practical range. A number of variables were identified as potentially influencing macroturbulence:

$$K_m, K_mS_m = fn\{y, H, k_s, B, U_o, g, \nu\}, \tag{3}$$

where the first four variables in the brackets are length scales (m) including distance from the boundary (y), flow depth (H), roughness height (k_s), and channel width (B); U_o is an appropriate velocity scale (m s^{-1}); g is gravitational acceleration (m s^{-2}); and ν is the fluid kinematic viscosity (m^2 s^{-1}). Eq. (3) assumes open channel flow in a rectangular channel in which the sidewall roughness is orders of magnitude smaller than the gravel bed roughness height (k_s). Eq. (3) also assumes that gravel particles at the bed are immobile. We assume consistency with Clauser's definition of an equilibrium boundary layer, and therefore use the friction velocity (u_*) as the velocity scale that is assumed constant (Clauser, 1954, 1956; Townsend, 1976). We performed dimensional analysis of Eq. (3) to arrive at a number of well-known dimensionless numbers for open channel flow over a gravel bed as

$$K_m l, \frac{K_mS_m}{u_*^2} = fn\left\{\frac{y}{H}, \frac{H}{k_s}, \frac{B}{H}, \frac{y}{k_s}, \frac{k_su_*}{\nu}, \frac{u_*}{\sqrt{gH}}\right\}. \tag{4}$$

l is used here to indicate any one of the length scales in Eq. (3) that might appropriately normalize the macroturbulence wavenumber, which is yet to be determined and is investigated in our results section. Scaling of the macroturbulence energy with the square of the friction velocity shown in Eq. (4) agrees with the most commonly reported spectral scaling in the literature and is an artifact of Clauser's boundary layer model (Perry and Abell, 1975; George and Castillo, 1997; Katul and Chu, 1998; Kim and Adrian, 1999; Nikora et al., 2001; Stewart and Fox, 2015). The dimensionless numbers on the right hand side of Eq. (4) include relative distance from the boundary (y/H), relative submergence (H/k_s), aspect ratio (B/H), relative distance above the roughness grains (y/k_s), roughness Reynolds number (k_su_*/ν), and the friction velocity ($u_*/(gH)^{0.5}$) scaled for open channel flow.

To arrive at a tractable set of experimental tests, we considered a number of controls to simplify the dependency of macroturbulence response variables upon the identified dimensionless numbers. First, we focused on measurements in the outer region, above the roughness layer, and therefore the equilibrium boundary layer could be examined in the outer region. We also collected data closer to the boundary elements, in the roughness layer, so that the beginning of the outer region could be visualized but emphasis was placed upon measurements

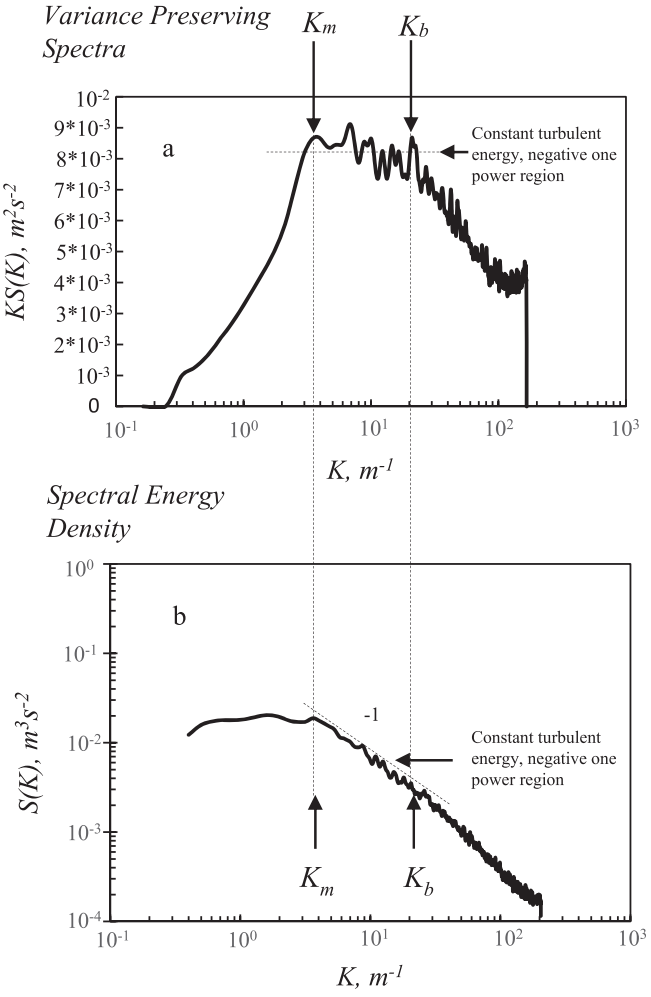

Fig. 1. Concept diagram of the macroturbulence wavenumber (K_m) and the bursting wavenumber (K_b) depicted in the variance preserving and spectral energy density for the streamwise velocity signal in (a) and (b), respectively. K_m and K_b bound the constant turbulent energy, negative one power region as is depicted in both the variance preserving spectra and the spectral energy density.

for $y > 2\ k_s$. Second, the relative submergence was always greater than five such that an outer flow region always existed for the study (Belcher and Fox, 2011). Third, the roughness type and height (k_s) was fixed for this study, which, while a limitation, allowed us to carefully investigate the sensitivity of the spectral approach and investigate variations based on the external energy input. Fourth, we focused on hydraulically rough open channel flow where the roughness Reynolds number is >70 (Nezu and Nakagawa, 1993); thus, removing the Reynolds number influence. Fifth, we considered subcritical, uniform, and steady open channel flow such that a gravitational interpretation of the friction velocity can be qualitatively gained (Hsu et al., 1998). Therefore, the last term on the right hand side of Eq. (4) is shown to be the energy gradient, which also reflects the Froude number if the Darcy-Weisbach relationship is invoked to substitute the depth-average velocity for the friction velocity. The assumption of $Fr < 1$ allows us to consider the impact of the energy gradient upon macroturbulence across the subcritical flow regime. With these simplifications in mind, we arrive at

$$K_m l, \frac{K_m S_m}{u_*^2} = fn\left\{\frac{y}{H}, \frac{B}{H}, S_e\right\}, \tag{5}$$

where S_e is the energy gradient and is equal to the bed slope for the case of uniform flow.

Eq. (5) suggests the potential for macroturbulence response variables to be dependent upon the relative distance from the boundary, the aspect ratio and the external energy gradient. The result of Eq. (5) was reasonable given previous macroturbulence results and our knowledge of turbulence energy production within equilibrium layers. Low-order dependence of turbulence kinetic energy upon the relative distance from the boundary has been shown to exist for the outer region of turbulence boundary layers (Perry et al., 1986; Nezu and Nakagawa, 1993), suggesting potential extension to the energy production associated with macroturbulence. Hypothesized dependence of macroturbulence upon the aspect ratio is plausible given that the weak secondary cells in flow over gravel are believed to be the averaged manifestation of instantaneous macroturbulence (Gulliver and Halverson, 1987; Belcher and Fox, 2009). The dependence of macroturbulence upon the energy gradient is reasonable given that spectral energy production has been suggested to be related to potential energy supplied externally (Katul and Chu, 1998). With these mechanisms in mind, the result in Eq. (5) was used to choose tests in a hydraulic flume with a gravel bed to quantify the scales of macroturbulence. We varied the slope and discharge in the hydraulic flume that enabled variation of $B\ H^{-1}$ and S_e. We designed and carried out the 11 tests shown in Table 1. (Note that all testing conditions and wavenumber results may also be found in the Supplemental table, Table 2) The 11 tests included three different slopes and four different flow depths for each slope. We could not collect data for the flow depth of 0.2 m at the slope of 0.006 due to the limitation of the head-box for our flume setup, so we had 11 tests instead of 12. For each test, we collected flow data at several vertical (y) locations across the flow depth (H), from 9 to 13 locations depends on the flow depth, thus allowing us to vary $y\ H^{-1}$ in Eq. (5).

Another consideration worthy of discussion for experiments specified in Table 1 was Shields number. The 11 tests provided a range of Shields number ($\tau^* = \tau[(\rho_s - \rho)gD]^{-1}$, where τ is the fluid shear stress, ρ_s is the sediment density, ρ is the fluid density, g is gravity, and D is the sediment grain size) from 0.0021 to 0.0998. The Shields number variation corresponds to values at or below the lifting threshold defined by Ling (1995), which has a minimum threshold value of approximately 0.1. The Shields number conditions for our tests reflect particles that are immobile at the bed (8 tests) or rolling along the bed (3 tests). However, we were concerned about damage to the velocimetry instrument during testing as well as further variability introduced by bed recontouring during transport, therefore we used an immobile bed for all tests. Using immobile bed conditions to study the turbulence flow structure is common in the literature (e.g. Hurther et al., 2007; Belcher, 2009; Belcher and Fox, 2009; Hardy et al., 2016; Bagherimiyab and Lemmin, 2018). The details of our experimental apparatus are discussed in the next section.

3. Methods

3.1. Data collection and time-average turbulence parameters

The experiments were performed in an adjustable-slope, recirculating flume that was 12 m long and 0.61 m wide as shown schematically in Fig. 2. The flume was made from fiberglass-resin panels and Plexiglas was used for its side walls (Belcher and Fox, 2009; Stewart and Fox, 2015). Immobile gravel roughness elements with $D_{50} = 0.0044$ and $D_{84} = 0.0056\ m$, where D_{50} and D_{84} are the sizes that 50% and 84% of particles are finer, respectively, composed the flume bed. Fig. 3 shows the particle size distribution used in this study. A 30 kW hydraulic pump was used to deliver water to the flume via a 20.3 cm supply line. A headbox was used to dissipate turbulence from the inflowing pipe. Just downstream of the headbox, a honeycomb device with 12.7 cm long by 6.4 mm diameter tubes was used to assist with providing rectilinear flow. Discharge was controlled by a gate-valve placed on the supply line. Data was collected at a test section placed 7.5 m downstream of the inlet where conditions were fully developed. Lastly, the testing section was sufficiently upstream of the outfall to provide uniform conditions within the test section.

Initially, instantaneous velocity data was collected with two instruments including a Sontek ADV and a Nortek Vectrino Profiler II ADV. Both instruments provided comparable and repeatable data (Ghasemi, 2016). The Nortek Vectrino Profiler II with a maximum sampling frequency of 100 Hz was chosen for data collection due to its higher sampling frequency and ability to collect an instantaneous profile. The Nortek Vectrino Profiler acoustic Doppler velocimeter (ADV from this point forward) measures the velocity of water for a range of locations 4.0 cm to 7.4 cm away from the probe transmitter. Data collected at a

Table 1
Experimental testing conditions.

Test	$S\ (mm^{-1})$	k_s (m)	$Q\ (m^3s^{-1})$	B (m)	$u^*\ (m\ s^{-1})$	τ^*	H (m)	y (m)	B/H	H/k_s	$Re\ (\times 10^4)$	K^+	Fr
1	0.0002	0.0112	0.021	0.61	0.0122	0.0021	0.1	0.001–0.08	6.10	8.93	2.6	67.78	0.35
2	0.0002	0.0112	0.046	0.61	0.0135	0.0026	0.133	0.001–0.11	4.59	11.87	5.3	75.20	0.50
3	0.0002	0.0112	0.068	0.61	0.0146	0.0030	0.167	0.001–0.147	3.65	14.91	7.2	81.17	0.52
4	0.0002	0.0112	0.085	0.61	0.0154	0.0033	0.2	0.001–0.13	3.05	17.86	8.4	85.92	0.50
5	0.0017	0.0112	0.038	0.61	0.0354	0.0176	0.1	0.001–0.08	6.1	8.93	4.7	197.49	0.64
6	0.0017	0.0112	0.062	0.61	0.0393	0.0217	0.133	0.001–0.11	4.59	11.87	7.0	219.25	0.67
7	0.0017	0.0112	0.092	0.61	0.0424	0.0252	0.167	0.001–0.147	3.65	14.91	9.7	236.55	0.70
8	0.0017	0.0112	0.12	0.61	0.0449	0.0283	0.2	0.001–0.18	3.05	17.86	12.2	250.38	0.72
9	0.006	0.0112	0.057	0.61	0.0666	0.0623	0.1	0.001–0.08	6.1	8.93	7.1	371.45	0.95
10	0.006	0.0112	0.085	0.61	0.0738	0.0765	0.133	0.001–0.11	4.59	11.87	9.7	411.89	0.92
11	0.006	0.0112	0.120	0.61	0.0843	0.0998	0.167	0.001–0.147	3.65	14.91	12.7	470.30	0.92

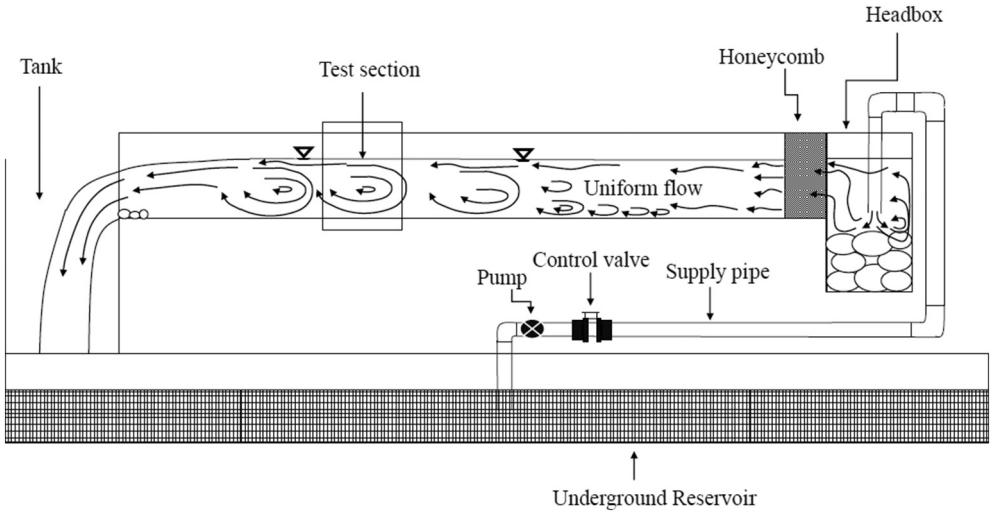

Fig. 2. Sketch of experimental setup.

single point 5 cm from the transmitter provided the highest correlation (COR) and signal-to-noise ratio (SNR) and was used for data analysis. However, the profile of velocity data was useful for providing order magnitude investigation of instantaneous velocity gradients.

Prior to collecting data with the ADV, the *Vectrino Profiler V1.32* software was used to perform a transducer test. The velocity amplitude and standard deviation were investigated to ensure consistency and stationarity. In addition, a probe check was always performed to produce long average amplitude versus range profiles for each of the four beams before data collection began; we ensured that the four profiles from the four beams were roughly the same, with similar peaks and shapes at the same range. During data collection, a rigid beam and a guide rod supported the ADV to prevent vibrations of the instrument.

Velocity data was collected with the down-looking orientation or the side-looking orientation depending on the distance from the bed. The orientation was changed due to constraints from the measurement control volume and submergence of the probe tip in water. As mentioned, the control volume of the ADV profiler used in this study was 5 cm below the probe's transmitter because this location minimized background disturbance and increased correlation. Also, the probe tip needed to be submerged in water to use the instrument for measuring water velocity. These two conditions required us to change the orientation from down-looking to side-looking to measure the water velocity near the free surface. The orientation was changed for the top 6 to 7 cm of the flow depth from down-looking to side-looking. We chose 1 to 2 cm more than the 5 cm threshold to ensure the probe stayed submerged in the case of any water surface fluctuations. For example, for the 10 cm of flow depth, the velocities with down-looking orientation were measured for y = 0 to y = 3.5 cm and side-looking orientation were measured for y = 4 cm to y = 10 cm. Table 3 details the distances from the bed when velocity measurements were collected with down-looking and side-looking orientations. The orientations specified in Table 3 were the same for all the different channel slopes we used in this study. A control module and quality control method was developed to check the orientation angle of the ADV and ensure accurate positioning in the vertical direction (Ghasemi, 2016). Data was only deemed acceptable if SNR > 15 and COR > 70. Data was collected at each point for 30 min with a 50 Hz sampling rate (n = 90,000 3D velocity data).

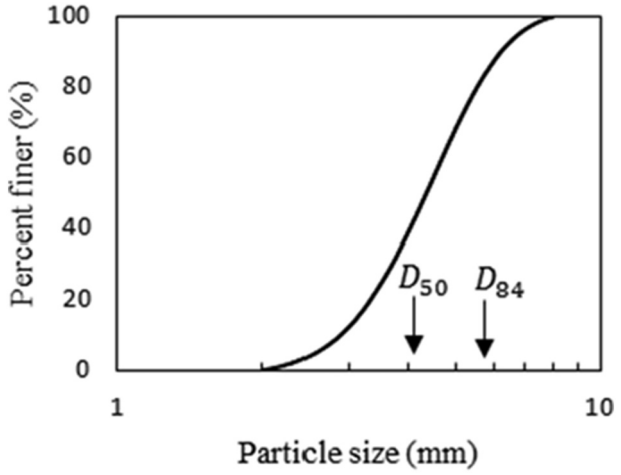

Fig. 3. Grain size distribution of bed used in this study.

The *Multi-instrument Turbulence Toolbox* (MITT) (MacVicar et al., 2014) was used to post-process the ADV data to ensure its quality and remove erroneous spikes due to acoustic reflections. A number of different filtering and despiking methods are provided in MITT, including the standard deviation method (MacVicar et al., 2014); the one side skewness method (MacVicar et al., 2014); the phase space method (Goring and Nikora, 2002); and the velocity correlation method (Cea et al., 2007). We did not find substantial differences between the despiking methods; therefore, the derivative-based phase space method was chosen because it not only worked well for despiking the data but was also independent of any fitting coefficients (Goring and Nikora, 2002).

Turbulence parameters derived from Reynolds-averaging the conservation of momentum, vorticity, and mechanical energy equations were analyzed for consistency with previously published semi-empirical laws and equilibrium theory. Our convention for the fluid's coordinate system used herein is as follows: u is the stream-wise direction of instantaneous velocity where positive values are in the direction of the streamwise mean, v is the vertical direction of instantaneous velocity where positive values are in the upward vertical, and w is the span-wise direction of instantaneous velocity where positive values follow the right-hand convention. Time-average velocities were calculated from the perturbation equations as.

$$u = U + u', \quad v = V + v', \quad \text{and} \quad w = W + w', \text{ where} \tag{6}$$

$$U = \frac{1}{n}\sum_{i=1}^{n} u_i, \quad V = \frac{1}{n}\sum_{i=1}^{n} v_i, \quad \text{and} \quad W = \frac{1}{n}\sum_{i=1}^{n} w_i \tag{7}$$

The primary normal and shear Reynolds stresses were calculated as.

$$RMS(u') = \left[\frac{1}{n}\sum_{i=1}^{n}(u_i - U)^2\right]^{0.5} \text{ and} \quad (8)$$

$$Rey(u'v') = \frac{1}{n}\sum_{i=1}^{n}(u_i - U)(v_i - V). \quad (9)$$

The vorticity equation provides further interpretation of the turbulent flow (Nezu, 2005), and therefore the anisotropy arising within the vorticity equation was calculated as

$$RMS(v')^2 - RMS(w')^2 = \frac{1}{n}\sum_{i=1}^{n}(v_i - V)^2 - \frac{1}{n}\sum_{i=1}^{n}(w_i - W)^2. \quad (10)$$

3.2. Spectral analyses to measure wavenumbers and energy

The energy spectrum was estimated using the discrete Fourier transform of the streamwise velocity. The computations were simulated in *Matlab Version R2014b*. Taylor's frozen hypothesis was used to convert spectral frequencies to wavenumbers ($K = 2\pi f U^{-1}$). Welch's algorithm and a Hanning window were used to produce ensembles of thirty time series for estimating the power spectrum at each location where 90,000 data were collected. Window overlap was not implemented and thus over-representation of data was avoided. We analyzed data with no filter and a low pass filter via three-point smoothing, as discussed below.

Emphasis was placed on the uncertainty and sensitivity of selecting the wavenumbers for macroturbulence and bursting (K_m and K_b), bounding the spectral production region. We found it was best to simultaneously use un-filtered and low-pass filtered spectra for both the spectral energy density plot and the variance preserving plot. This approach was performed to identify K_m and K_b (Figs. 4 and 5, respectively). The un-filtered plots allowed consistent visualization of the spectral production region as a negative one slope region in the spectral energy density plot and as a constant turbulence kinetic energy region in the variance preserving spectra. However, the noise within the un-filtered spectra made it difficult to identify pronounced peaks that might be associated with the imprint of macroturbulence and bursting. The filtered spectra alleviated the problem by allowing visualization of consistent peaks whereby the spectral production region was bounded. However, the filtered spectra had the disadvantage of producing spectral energy density that fall away from the negative one slope line near their boundaries due to the filtering function. In some cases, this caused confusion such that the actual peak associated with the imprint of macroturbulence and bursting could be misidentified if only filtered spectra was used. Therefore, using all four plots simultaneously alleviated problems in our selection of K_m and K_b. As there is some subjectivity in visually choosing the bounding wavenumbers, we placed uncertainty in our measurements of K_m and K_b. On average, the full range of the wavenumbers was ±25% and ± 11% of the chosen central values of K_m and K_b, respectively. We also investigated the sensitivity of K_m and K_b results to the time duration of velocity data used to analyze the spectra.

The spectral production region was present with distinct boundaries for 85% of the locations where velocity data was collected, which was consistent with the work of others (see review in Katul and Chu, 1998). The locations where the spectral production region was not present were data collected with the lowest energy gradient (S = 0.0002 m m^{-1}, Tests 3 and 4) and locations far from the bed. For the test with a flow depth equal to 16.7 cm, the spectral production region was not present for the six locations corresponding to $y \geq 8$ cm

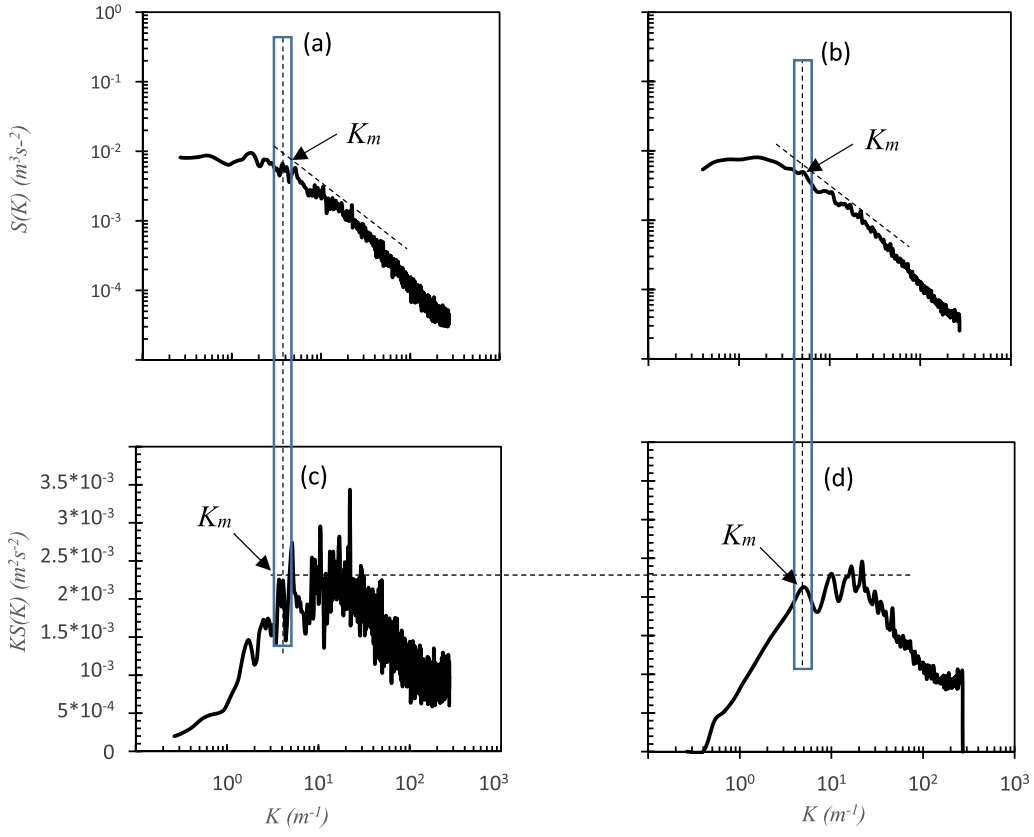

Fig. 4. Identifying K_m including: (a) non-filtered spectral energy density, (b) filtered spectral energy density, (c) non-filtered variance preserving spectra, and (d) filtered variance preserving spectra. The blue box shows the range of uncertainty involved in identifying K_m.

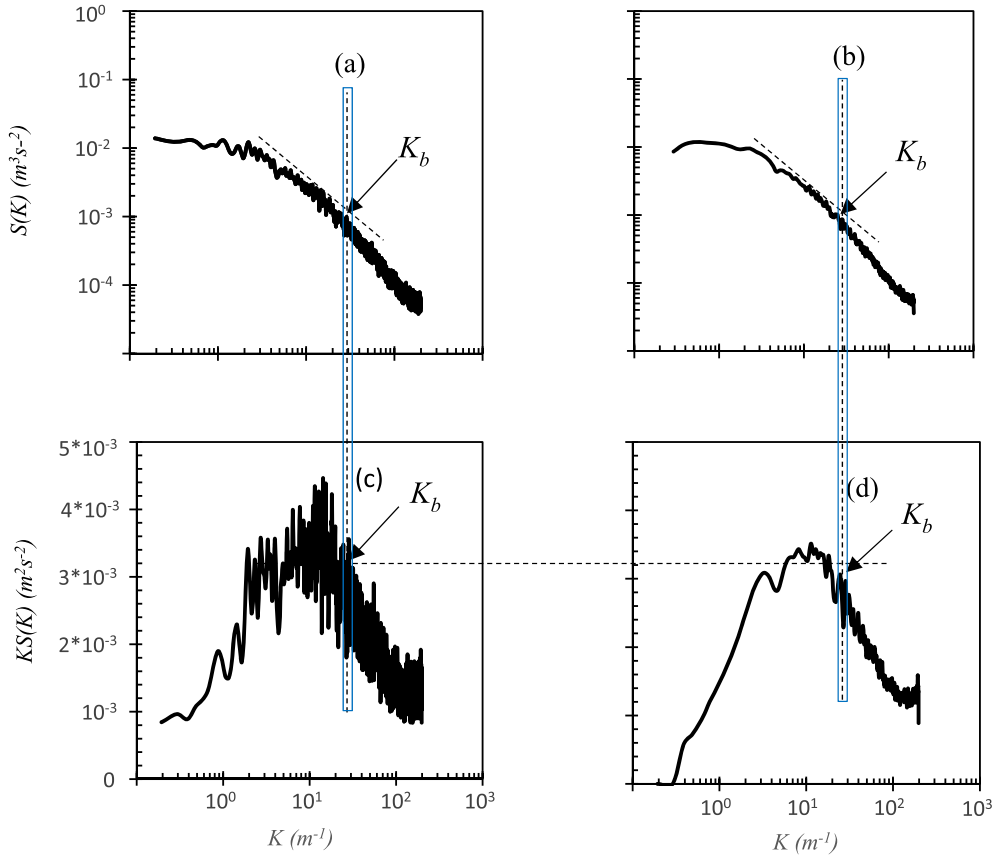

Fig. 5. Identifying K_b including: (a) non-filtered spectral energy density, (b) filtered spectral energy density, (c) non-filtered variance preserving spectra, and (d) filtered variance preserving spectra. The blue box shows the range of uncertainty involved in identifying K_b.

($y\,H^{-1} \geq 0.5$). For the test with a flow depth equal to 20 cm, the spectral production region was not present for the eight locations corresponding to $y \geq 4.5$ cm ($y\,H^{-1} \geq 0.23$). The lack of the spectral production region far from the boundary for flows with weak energy inputs has been associated with a balance of turbulence energy production and turbulence transfer within the flow (Tchen, 1953; Katul and Chu, 1998). We found that locations lacking the spectral production region also had very low turbulence production and transfer, which were of the same order of magnitude.

3.3. Scaling wavenumbers and energy

We tested scaling K_m and K_b with inner and outer variables against the hydraulic parameters in Eq. (5). Studies of fully turbulent flow in open channels have tended to normalize the spectral wavenumbers with inner variables as opposed to outer variables (Katul and Chu, 1998; Nikora, 1999, 2005), although scaling of the bursting period has been suggested using outer and mixed variables (Nezu and Nakagawa, 1993; Demare et al., 1999). Past equilibrium boundary theory developed using conceptual and theoretical grounds for other flow cases, such as pipeflow, has tended to suggest that the largest production scale (i.e., K_m) scales best with an outer scale while the smaller production scale (i.e., K_b) scales best with inner variables (Perry et al., 1986; Kim and Adrian, 1999). Therefore, we tested both the inner and outer length scales as potentially appropriate for scaling the macroturbulence and bursting wavenumbers. We then used the wavenumbers to calculate the macroturbulence and bursting periods, and the latter was compared with existing published formulae.

We tested scaling the macroturbulence energy with formulae that account for systematic variation of the hydraulic parameters in Eq. (5). The most common and traditional scaling of the spectral signal of the streamwise velocity is the friction velocity, and therefore we test the scaling of macroturbulence energy with the friction velocity. However, friction velocity scaling does not account for variation in macroturbulence energy as a function of the terms in the brackets of Eq. (5). Given the ubiquitous nature of macroturbulence, we test scaling macroturbulence energy with laws that consider the variation of turbulence kinetic energy in the flow field.

To arrive at scaling that considers the turbulence energy laws, we used the definition of the streamwise turbulence kinetic energy of the fluid ($\overline{u'^2}$) as

$$\frac{\overline{u'^2}}{u_*^2} = \frac{1}{u_*^2}\int_0^\infty KS(K)d(\log(K)). \tag{11}$$

Considering the existence of the spectral production region bounded by the macroturbulence and bursting wavenumbers, Eq. (11) can be further discretized as

$$\frac{\overline{u'^2}}{u_*^2} = \frac{1}{u_*^2}\left[\int_0^{K_m} KS(K)d(\log(K)) + \int_{K_m}^{K_b} KS(K)d(\log(K)) + \int_{K_b}^{\infty} KS(K)d(\log(K))\right]. \tag{12}$$

Eq. (12) can be divided by the left-hand-side to yield unity as

$$1 = \left[\frac{\int_0^{K_m} KS(K)d(\log(K))}{\overline{u'^2}}\right] + \left[\frac{\int_{K_m}^{K_b} KS(K)d(\log(K))}{\overline{u'^2}}\right] + \left[\frac{\int_{K_b}^{\infty} KS(K)d(\log(K))}{\overline{u'^2}}\right]. \tag{13}$$

Eq. (13) represents the relative contribution of the spectral regions to the total energy, and the regions have been conceptualized (Perry et al., 1986; Nezu and Nakagawa, 1993) as containing turbulence motions that can be represented as

$$1 = [\text{Largest scale motion}] + [\text{Production}] + [\text{Transfer and Dissipation}]. \quad (14)$$

We focus on the spectral production region to estimate the fraction of the spectral production energy, *SPE*, of the overall turbulence kinetic energy as

$$SPE = \frac{\int_{K_m l}^{K_b l} Kl\, S(Kl) d(\log(Kl))}{\overline{u'^2}}, \quad (15)$$

where l is the appropriate length scale. Physical considerations have shown us that the spectral production region is variance preserving such that energy is constant. Therefore, we can replace the constant energy with the energy of macroturbulence and simplify Eq. (15) to arrive at

$$SPE = \frac{K_m l\, S(K_m l)}{\overline{u'^2}} \int_{K_m l}^{K_b l} d(\log(Kl)). \quad (16)$$

The bursting wavenumber is an order of magnitude greater than the macroturbulence wavenumber, and therefore the integral in Eq. (16) reduces to unity to arrive at

$$SPE = \frac{K_m l\, S(K_m l)}{\overline{u'^2}}. \quad (17)$$

Eq. (17) states that the macroturbulence energy can be appropriately normalized with the measured streamwise turbulence kinetic energy for the equilibrium outer region. The normalization is shown in the results section.

The result in Eq. (17) allowed us to impose two additional potential scaling laws for the macroturbulence energy. Eq. (17) also allowed us to test if relationships that can predict the streamwise turbulence kinetic energy ($\overline{u'^2}$) might prove useful for scaling the macroturbulence energy. We test this concept by considering two such scaling methods that parameterize the streamwise turbulence kinetic energy as logarithmic and exponential functions defined as.

$$\frac{\overline{u'^2}}{u_*^2} = c_1 - c_2 \ln\left(\frac{y}{H}\right) - c_3 \left(\frac{y u_*}{\nu}\right)^{-\frac{1}{2}} \text{ and} \quad (18)$$

$$\frac{\overline{u'^2}}{u_*^2} = c_4^2 \exp\left(-\frac{y}{H}\right)^2, \quad (19)$$

where c_i are empirical coefficients.

Eq. (18) was derived by Perry and coworkers with the most comprehensive treatment of the function reported in Perry et al. (1986). Eq. (18) was derived by hypothesizing that the streamwise turbulence energy could be distributed such that a portion of the flow is defined based on inner-flow scaling, a portion of the flow is defined based on outer-flow scaling, and the spectral production region is a region of overlap where both inner and outer scaling are valid (Perry and Abell, 1975). The first two terms on the right hand side of Eq. (18) were also derived by invoking Townsend's attached-eddy hypothesis, assuming that the geometry and topology of the eddies could be described with hairpin vortices, and hypothesizing the continuous distribution of hairpin hierarchies, where hierarchies are an array of hairpins at different stages of development and the length scale of the hierarchies varies continuously from a smallest, inner length scale to a largest, outer length scale (Perry and Chong, 1982). Scaling the macroturbulence energy can be accomplished by considering Eq. (17) and recognizing that logarithmic term in Eq. (18) is explicit to the spectral production region and arriving at

$$SPE = \frac{K_m l\, S(K_m l)}{\left[c_1 - c_2 \ln\left(y H^{-1}\right)\right] u_*^2}. \quad (20)$$

Eq. (20) suggests that macroturbulence energy can be appropriately scaled with a logarithmic function, and we test the scaling in our results section.

Eq. (19) was derived by Nezu and Nakagawa (1993) where they invoked the equilibrium boundary layer assumption. Those authors integrated the turbulence energy budget after considering that turbulence energy is in equilibrium and thus turbulence generation is equal to dissipation (Nezu and Nakagawa, 1993, pp. 24). Scaling the macroturbulence energy can be accomplished by considering Eqs. (17) and (19) as

$$SPE = \frac{K_m l\, S(K_m l)}{c_4^2 \exp\left(-y H^{-1}\right)^2 u_*^2}. \quad (21)$$

Eq. (21) suggests that macroturbulence energy can be appropriately scaled with an exponential function based on energy equilibrium, and we test the scaling in the results section.

4. Results

4.1. Data collection and time-average turbulence parameters

Quality assurance of the turbulence dataset and adherence to our equilibrium and double-layer assumptions was assessed by scaling the primary mean velocity with both inner and outer variables (see Fig. 6). Inner scaling showed a very weak to no wake for the velocity profiles, and therefore the velocity law for hydraulically rough flows (Hsu et al., 1998) fit well with the data (see Fig. 6a; the law is also included in the figure). Outer scaling via the velocity defect was investigated (see Fig. 6b, c) where the selection of the velocity scale as U_{max} or u_* invokes asymptotic invariance equilibrium (George and Castillo, 1997) or Clauser equilibrium (Clauser, 1954, 1956). Both equilibrium definitions collapsed the data well, and the equilibrium results are notable given that the energy input varies by two orders of magnitude across the 11 hydraulic conditions.

The primary Reynolds shear stress, primary normal stresses and turbulence stress anisotropy also scaled well with the friction velocity consistent with hydraulically rough flow over a gravel bed (Kironoto et al., 1994; Rodríguez and García, 2008). Shear stress scaled well with the uniform flow law for turbulent open channels (Fig. 6d). The primary normal stresses also scaled well with the friction velocity (Fig. 6e) and collapsed well as the relative turbulence intensity (Fig. 6f), where the former conforms to the equilibrium definition and the latter suggests the consistency of turbulence measurements across the velocity datasets.

The turbulence dataset shows consistency of time-average turbulence results with existing relationships derived using the equilibrium boundary layer assumption. The outer region data results show well-defined time average characteristics including, a near-logarithmic distribution of the streamwise velocity in the vertical, a near-linear distribution of the primary Reynolds shear stress, and weak exponential decay of the primary normal stresses with depth (Nezu and Nakagawa, 1993; Nezu, 2005; Nikora and Roy, 2012; Stewart and Fox, 2015). Scaling of the time-average results via laws derived with the equilibrium assumption provides support for existence of equilibrium in the experimental flume. In this sense, results are consistent the equilibrium definition in which the outer region shows a balance of turbulence generation and dissipation (Nezu and Nakagawa, 1993).

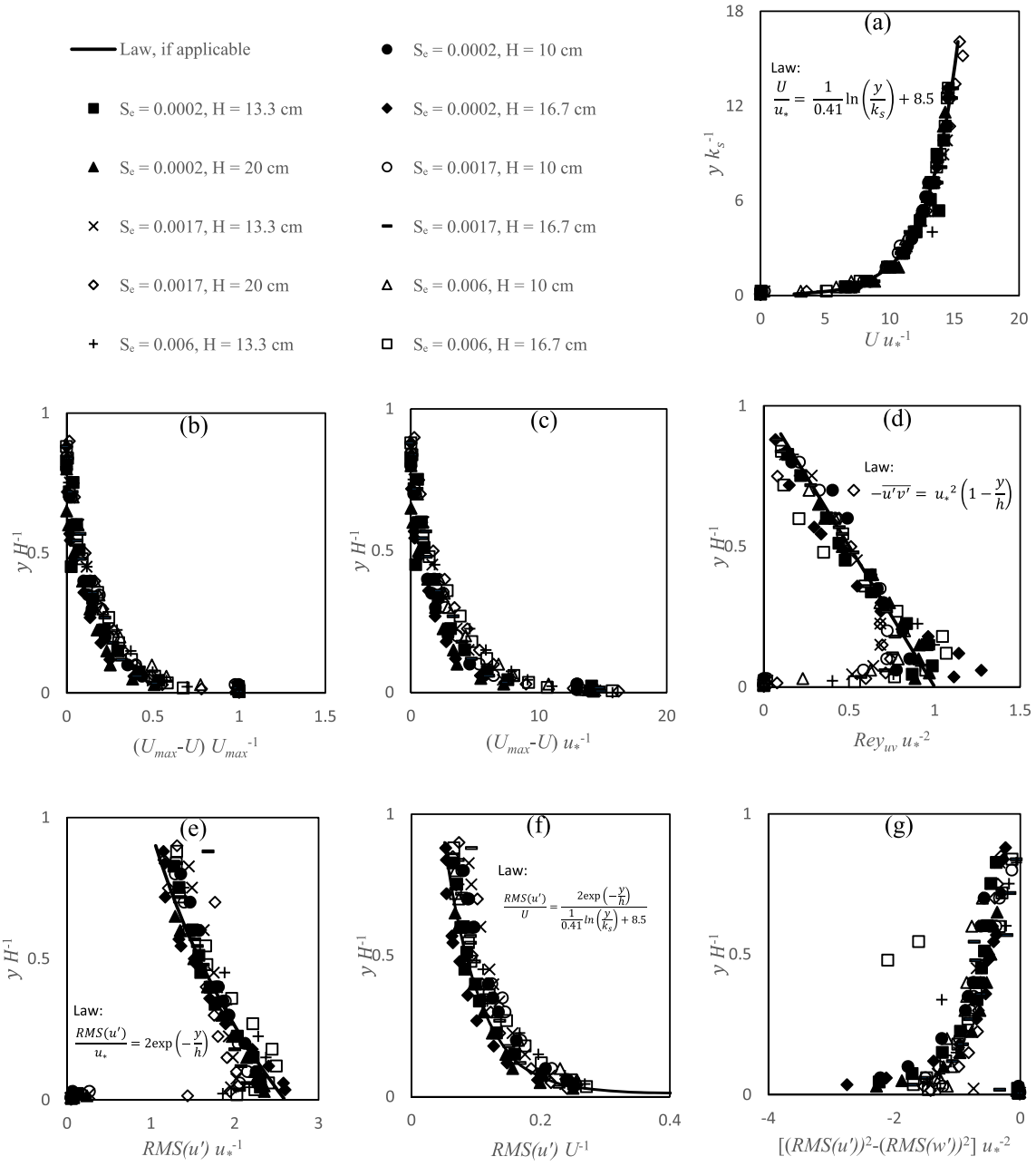

Fig. 6. Consistency of time-average results with existing equilibrium derived laws. Time-average turbulence for the experimental tests including: (a) inner scaling of the mean velocity, (b) outer scaling of the mean velocity with the freestream velocity, (c) outer scaling of the mean velocity with the friction velocity, (d) the primary Reynolds shear stress, (e) the primary normal stress, (f) the relative turbulence intensity, and (g) turbulence anisotropy.

Turbulence stress anisotropy was found to exist throughout the flow depths of the experiments (Fig. 6g). The anisotropy results highlight the weak production of secondary currents which is now a well-recognized feature of open channel flow over a gravel-bed regardless of the aspect ratio (Albayrak, 2008; Rodríguez and García, 2008; Belcher and Fox, 2009; Nikora and Roy, 2012). The weak secondary cells within flow over gravel are believed to be the time-averaged imprint of the instantaneous macroturbulence whereby the coherent structures are self-organized laterally as a result of near-corner coherency, bed roughness, and bursting (Gulliver and Halverson, 1987; Albayrak, 2008; Belcher and Fox, 2009; Nikora and Roy, 2012). In the present dataset, secondary velocities were one to two orders of magnitude less than the primary velocity. Secondary energy fluxes were even smaller with secondary production being three to four orders of magnitude smaller than primary production.

Taken together, time-average results support the equilibrium and double layer hypotheses for the dataset assumed in our design. Time-average results show logarithmic streamwise velocity and near-linear shear stress distributions suggesting equilibrium for the outer region. The anisotropy results are consistent with the underlying presence of bursting and macroturbulence reflecting a turbulence double-layer.

4.2. Spectral analyses to measure wavenumbers and energy

The sensitivity of macroturbulence and bursting wavenumbers results shows that K_m required over 17 min to stabilize (Fig. 7a), longer

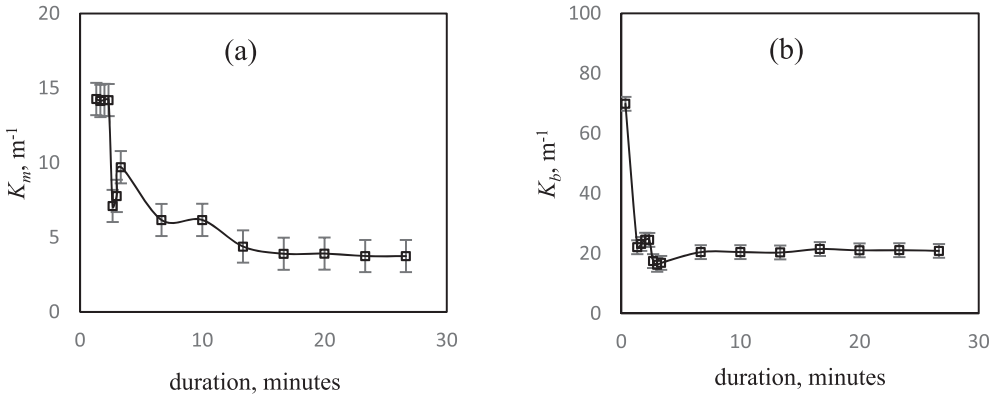

Fig. 7. Results of the sensitivity of selecting the macroturbulence wavenumber and bursting wavenumber (K_m and K_b). K_m and K_b are plotted in (a) and (b), respectively, as a function of the number of velocity measurements collected and analyzed using the spectral analyses. Data was collected at 50 Hz therefore the total n corresponds to 26.7 min of continuous data.

than suggested turbulence time series (Nikora and Goring, 2000; Fox, 2002; Buffin-Bélanger and Roy, 2005). K_b required approximately 7 min to stabilize. The 17 and 7 min sampling durations corresponded to 50,000 and 20,000 data points for the sampling rate in the sensitivity experiment. In order to be conservative in our study, 30-min data collection duration was used at each location to estimate K_m and K_b.

These sensitivity results show that a rather long time series (>17 min) at a single point is suggested for convergence and stationarity of K_m and K_b, which contradicts the conventional wisdom that just a few minutes of turbulence data is sufficient for measuring characteristics of turbulence. The reason for the result reflects the rate at which macroturbulence passes the velocity sensor. The macroturbulence period (T_M) in the outer region varied on the order of a second (see next section) and, depending on the mean streamwise velocity and flow depth, we were able to collect one to two thousand repetitions of a macroturbulence cycle that passes the velocity probe since we collected data for 1800 s.

4.3. Scaling wavenumbers and energy

We tested both the inner and outer length scales as potentially appropriate for scaling the macroturbulence and bursting wavenumbers. Results suggest both wavenumbers scale best with the outer variable (H) above the roughness region of the flow (Fig. 8). Macroturbulence and bursting wavenumbers approached a constant value when scaled with the flow depth (H) with changing yH^{-1} for the most of the outer region. The mean values of the outer scaled wavenumbers were $K_mH = 0.48$ and $K_bH = 3.4$ when calculated using data above the roughness layer ($y\,k_s^{-1} > 2$). Both wavenumbers show a lack of constancy and an increasing trend with yH^{-1} when scaled with the inner variable. K_mH was approximately an order of magnitude smaller than K_bH, reflecting an order of magnitude larger length scale for macroturbulence compared to bursting. Both wavenumbers showed consistency with one another in terms of their distribution with yH^{-1} regardless of the scaling applied suggesting a physical relationship between the turbulence scales.

Next, we turned our attention to macroturbulence energy. The non-scaled macroturbulence energy, $K_mS(K_m)$, was found to vary consistently with energy input and yH^{-1} (Fig. 9a). We normalized $K_mS(K_m)$ via Eq. (17) when the macroturbulence energy is collapsed with the measured streamwise turbulence kinetic energy at each measurement location in the equilibrium outer region. We found the normalization result in Eq. (17) to hold true for the current dataset (Fig. 9b) as the streamwise turbulence kinetic energy collapsed the macroturbulence energy well and removed the dependence of the energy upon yH^{-1}. The result validated the assumptions in Eqs. (11) through (17) including the order of magnitude difference between bursting and macroturbulence wavenumbers, which was also verified in Fig. 8. The scaled macroturbulence energy reaches a constant value of 0.25 in Fig. 9b. Considering Eq. (14), the results imply that turbulence energy associated with production provides a constant contribution on the order of 25% to the total turbulence energy, regardless of the energy input.

We tested scaling the macroturbulence energy with the friction velocity, the logarithmic scaling in Eq. (20), and the exponential scaling in Eq. (21). Scaling with the friction velocity accounted for the external energy input to some degree but the macroturbulence energy still showed pronounced variation with yH^{-1} (Fig. 9c). Both the logarithmic and exponential scaling helped remove dependence on yH^{-1} (Fig. 9d, e).

5. Discussion

The scaling results are discussed in relationship to the experimental design. We then present and discuss implications and transferability of novel predictive equations for macroturbulence. Finally, a time parameter to consider when designing macroturbulence experiments is presented and discussed.

The scaling results simplify the dependence of macroturbulence wavenumber and energy on hydraulic parameters tested in the experimental design (see Eq. (5)). For these experiments over a gravel bed, macroturbulence and bursting wavenumbers were centered around a constant value in the outer region when scaled with the outer variable (i.e., the flow depth). Specifically, the outer scaled macroturbulence wavenumber (K_mH) averaged 0.48 and was independent of yH^{-1}, BH^{-1}, and S_e (see Fig. 8). While to our knowledge, an experiment that varies yH^{-1}, BH^{-1}, and S_e to measure macroturbulence variation is not present in the literature, the scaling results in Fig. 8 are corroborated by comparison with past studies that report macroturbulence variation with the flow depth (see Table 1 in Roy et al., 2004). For comparison with the literature, we compute the average length of a macroturbulence cycle equal to the inverse of the wavenumber. Results of the experiments herein had a streamwise length range of 0.6H to 4.6H and mean value of 2.3H. These results are nearly equal to the cross-study range of 1H to 6H and mean of 2.5H calculated for the nine peer-reviewed studies discussed in Roy et al. (2004). This comparison lends confidence to these results. One significant finding of this study is that the length scales were found to be independent of distance above the boundary, aspect ratio, energy gradient, Froude number, or Shield's parameter.

Data results from this study show that macroturbulence energy scales with the streamwise turbulence kinetic energy. The data scaling results are in agreement with our theoretical derivation of the macroturbulence energy scaling (see Eq. 17) where we invoke: the

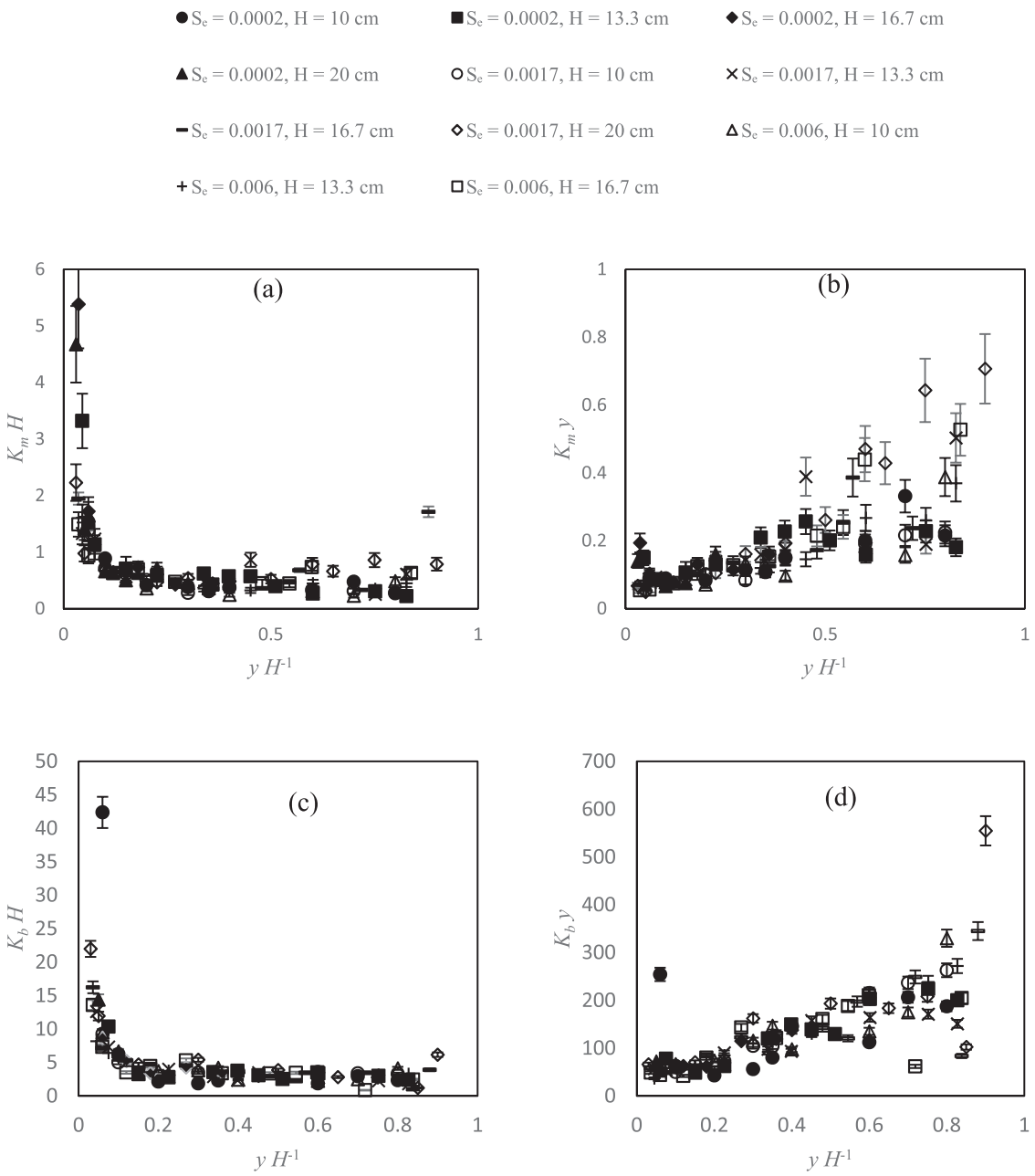

Fig. 8. Scaling of the macroturbulence and bursting wavenumbers (K_m and K_b) with inner and outer variables. (a) Scaling K_m with H, (b) scaling K_m with y, (c) scaling K_b with H and (d) scaling K_b with y.

spectral definition of the turbulence kinetic energy; the constant turbulence energy of the −1 spectral power region; and the order of magnitude difference between the bursting and macroturbulence wavenumbers. The energy finding in this paper is significant because an appropriate model-equation for streamwise turbulence kinetic energy can then be used to scale macroturbulence energy. We illustrate this point by scaling macroturbulence energy with two semi-theoretical model-equations for turbulence kinetic energy commonly applied in turbulence studies, including logarithmic and exponential functions. The energy shows neither dependence on BH^{-1} nor additional dependence on S_e (Fig. 9). The lack of dependence on the aspect ratio may be indicative of weak secondary currents (see Section 4.1).

Based on the macroturbulence scaling results, predictive equations for macroturbulence time and energy scales are presented for the first time, to our knowledge. The transferability and implications of the predictive equations is then discussed.

An equation for the macroturbulence time period is defined with outer variables, and the bounds on the coefficient are fitted to the experimental dataset reported herein. We used the outer scaled spectral wavenumbers for macroturbulence (K_mH) and bursting (K_bH) to calculate the macrotubulence period (T_m) and bursting period (T_b). The bursting period found using our dataset was compared against the commonly cited bursting period defined using outer variables specified using the threshold quadrant technique by Nezu and Nakagawa (1993) (Eq. (8.29) in Nezu and Nakagawa, 1993) as

$$T_b = (1.5 \text{ to } 3)\frac{H}{U_{max}}. \tag{22}$$

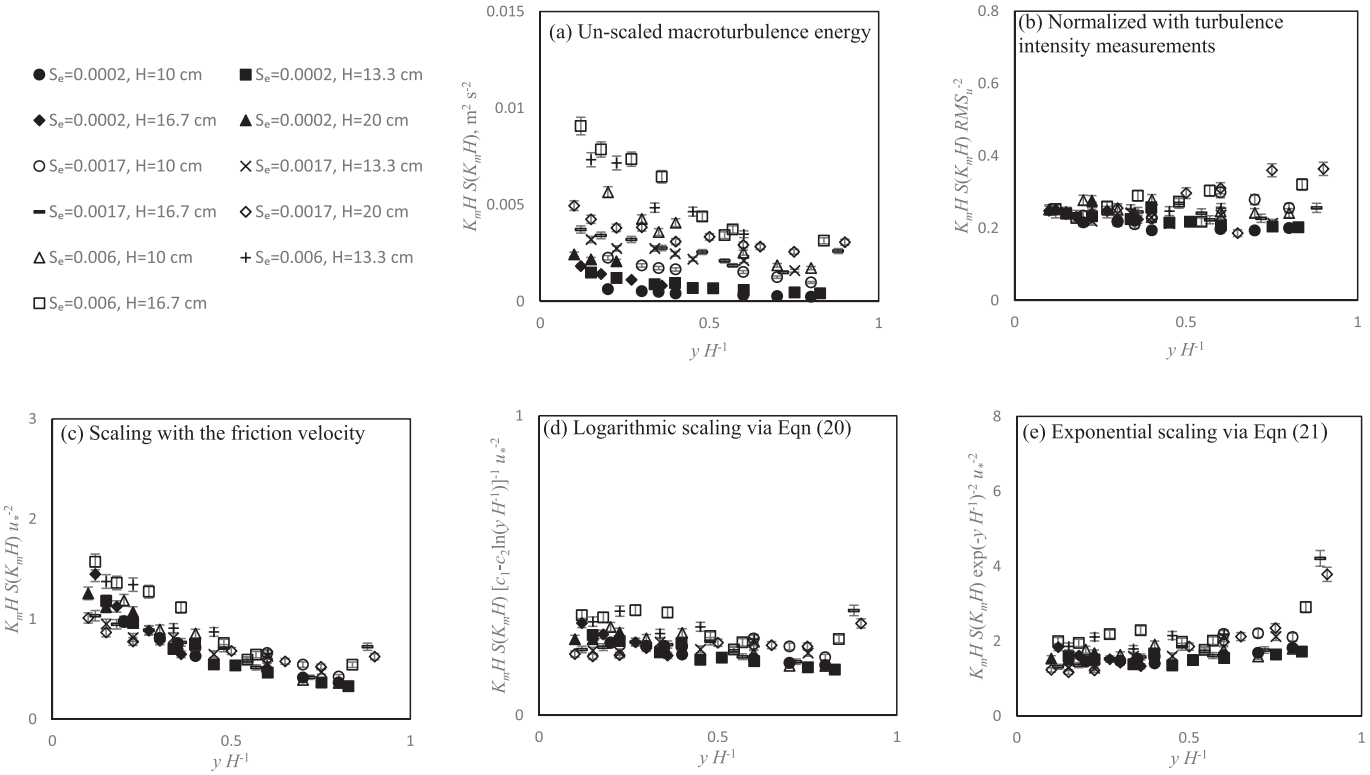

Fig. 9. Scaling of macroturbulence energy for the outer region of the hydraulically rough open channel flow.

Results show that the suggested range in Eq. (22) bounded the spectral measurements calculated with K_bH very well (see Fig. 10a). Analogous bounds were placed on the macroturbulence period (K_mH) in which the bounds were specified to contain 90% of the data-derived periodicity (Fig. 10b). In this manner, a relationship was established for the macroturbulence period as

$$T_m = (9 \text{ to } 27)\frac{H}{U_{max}}. \tag{23}$$

Eq. (23) highlights the order of magnitude difference between the bursting period and macroturbulence period, yet the results in Fig. 10 also highlight the consistency of the turbulence scales with one another. We suggest that Eq. (23) has high potential for transferability to other studies due to: the consistency of data results herein with cross-study average macroturbulence scales (Table 1 in Roy et al., 2004); the consistency of the bursting period results reported herein with bursting period formulae derived from cross-study analyses (Eq. (8.29) in Nezu and Nakagawa, 1993); and consistency of the order of magnitude difference reported between the two scales with visualization of coherent structures over gravel beds (Hurther et al., 2007; Belcher and Fox, 2009; Hardy et al., 2016).

Predictive equations for the macroturbulence energy are also considered. Macroturbulence energy scales with streamwise turbulence kinetic energy and Eq. (17) is re-written as

$$K_mH\, S(K_mH) = SPE\, \overline{u'^2}. \tag{24}$$

SPE was 0.25 for this study and Eq. (24) is re-written omitting the scales as

$$K_m\, S(K_m) = 0.25\, \overline{u'^2}. \tag{25}$$

Fig. 11a shows Eq. (25) (x-axis) plotted against the data (y-axis) collected in this study, and the excellent fit is observed. Eq. (25) has some transferrable qualities given the theoretical derivation of the macroturbulence energy scaling in Eq. (17). However, the contribution of macroturbulence energy to the total turbulence energy (i.e., *SPE*) could use further investigation across other gravel-bed studies since this was the first study, to our knowledge, to report this value. Also, a universal equation for streamwise turbulence kinetic energy is still somewhat an open topic for gravel-bed studies. An exponential function for macroturbulence energy is written by considering Eq. (21) as

$$K_m\, S(K_m) = SPE\, c_4^2\, \exp\left(-y\, H^{-1}\right)^2 u_*^2. \tag{26}$$

Fig. 11b shows Eq. (26) plotted against the data collected in this study. The empirical coefficient of $c_4 = 2.5$ was fitted, which is slightly higher than the values of 2.3 and 2.04 reported by Nezu and Nakagawa (1993) and Kironoto et al. (1994), respectively. The logarithmic-based equation for macroturbulence energy is written by considering Eq. (20) as

$$K_m\, S(K_m) = SPE\, \left[c_1 - c_2 \ln\left(y\, H^{-1}\right)\right] u_*^2. \tag{27}$$

Fig. 11c shows Eq. (27) plotted against the data collected in this study. The empirical coefficients equal to 1.9 and 1.32 from Nikora and Goring (2000). Both exponential and logarithmic equations show reasonable prediction for macroturbulence energy. The transferability of the equation's exponential or logarithmic function will require some justification for a given application, at this time, given the semi-theoretical nature of the formula. Empirical evidence is mixed between the best fitting of the exponential and logarithmic functions for studies of flow over a gravel-bed. Kironoto et al. (1994) show good fit for the exponential function. Nikora and Goring (2000) show the logarithmic

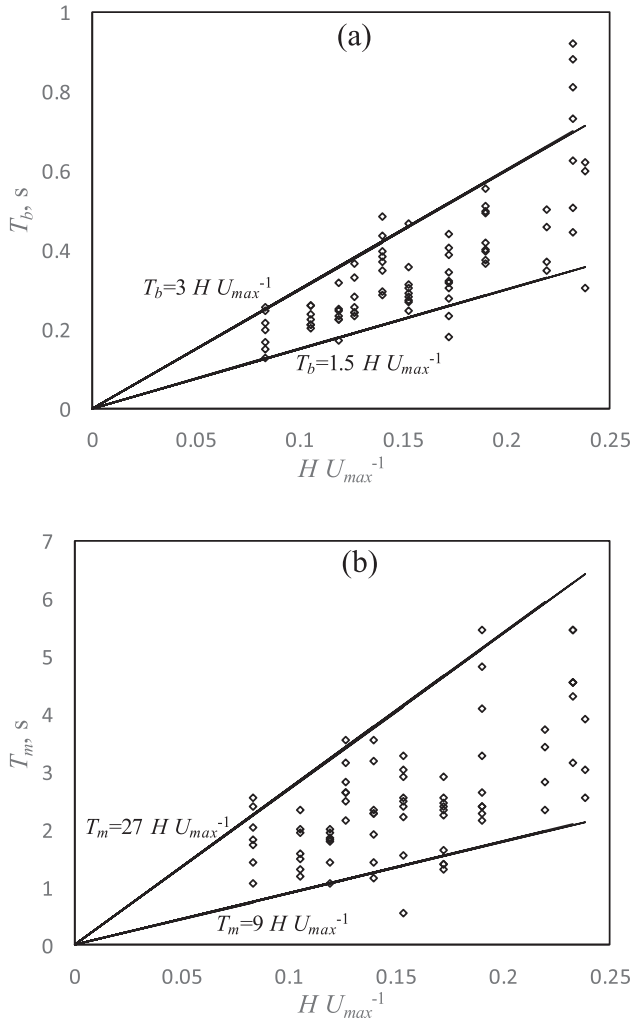

Fig. 10. (a) The bursting period (T_b) above the roughness layer for the experiments in Table 1. T_b was calculated using K_b identified with the four-plot spectral method. The lines plotted are the suggested bounds shown in Eq. (8.29) in Nezu and Nakagawa (1993). (b) The macroturbulence period (T_m) above the roughness layer plotted similarly as for the bursting period. The lines plotted contain 90% of the data.

function is a better fit and the exponential function under-predicts streamwise turbulence kinetic energy farther from the gravel bed. Tritico and Hotchkiss (2005) show the exponential function under-predicts turbulence kinetic energy while the logarithmic function over-predicts turbulence kinetic energy farther from the gravel-beds. Rodríguez and García (2008) show the exponential function fits better and the logarithmic function over-predicts turbulence kinetic energy farther from the wall. Given the lack of universality for a streamwise turbulence kinetic energy formula for flow over gravel-beds, we recommend the appropriateness of an exponential or logarithmic function for turbulence kinetic energy be justified prior to applying Eq. (26) or (27) for macroturbulence energy prediction. Nevertheless, results are encouraging that we might work towards constraining formula for macroturbulence energy.

Implications of the results in Eqs. (23), (26) and (27) suggest an approach to predict the timescales and energy of macroturbulence for linking river turbulence with sediment transport applications. For example, we postulate macroturbulence energy equations could predict the fluid's capacity to carry fluvial sediment in the outer region of the flow. The largest eddies have long been considered responsible for carrying fluvial sediment in the outer region (Nezu and Nakagawa, 1993). However, in practice, the transport capacity based on stream power (e.g., $\tau\ U$, $\tau^{1.5}$, or U^3) or similar velocity power laws still provide the prevailing method for estimating non-uniform suspended sediment transport. Predicting the sediment carrying capacity via macroturbulence formula suggests one application to potentially help close the gap between turbulence and fluvial sediment transport.

Implications of the results for the turbulence double layer are also meaningful, and scaling results (Fig. 8) suggest connectivity of wall-driven bursting and macroturbulence. Turbulence energy of eddies associated with macroturbulence and bursting are nearly equal to one another (Fig. 1) and allows for speculation that they are different regions of the same highly connected structure. This concept is inferred by Roy et al. (2004) in their fluid coherency observations in a gravel bed river and suggests a coupled structure for the tornado-like macroturbulence and the near-bed shedding process off the leeside of pebbles. The work of Belcher and Fox (2009) for gravel bed using turbulence decomposition and topological analysis via critical point theory further corroborates the connectivity concept as the source/sink analysis of the macroturbulence and bursting vortical components suggest the transfer of turbulence momentum from the large scale to the small scale, and vice versa. The flow visualization of Shvidchenko and Pender (2001) also tends to qualitatively support this idea as small tubes associated with bursting tend to be embedded and connected within the macroturbulence motion. Intermediate mechanisms that facilitate energy sharing and connectivity of wall-driven bursting and macroturbulence are less clear and require further investigation. A number of postulated intermediate mechanisms fueling energy sharing and connectivity are: (i) the classical lift of near bed eddies and eddy packets to transport turbulence energy vertically to macroturbulence (Hurther et al., 2007), (ii) the less studied helicity of macroturbulence as well as the time-averaged motions associated with secondary currents that will help to transfer energy in three dimensions (Nikora and Roy, 2012, pp. 11), and (iii) the less studied manifestation of bursting turbulence in free surface fluctuations that could cause instantaneous non-uniform flow and secondary energy production at the macroturbulence scale (Horoshenkov et al., 2013; Stewart and Fox, 2015).

Implications regarding comparison with other turbulence boundary layer flows are also possible, although scaling of macro-sized coherency has been found to vary across boundary layer types and Reynolds numbers (Monty et al., 2009; Guala et al., 2011). The dependence of macroturbulence on outer scaling show agreement with turbulence boundary layer studies at high Reynolds numbers where very large scale motion and superstructures persist across the entire boundary layer vertically and strongly interact with near-wall turbulence (Hutchins and Marusic, 2007). This class of high Reynold's numbers flows, including our hydraulically rough open channel flow reported herein, contradicts results showing the separation of near-wall and outer region scales at lower Reynold's numbers (Guala et al., 2011).

Finally, we discuss a time parameter to consider when designing macroturbulence experiments. Our method sensitivity result showed a rather long time series on the order of 17 min of data at a single point was needed to achieve convergence of the macroturbulence wavenumber. In some instances, it has been shown that 1 min or just a few minutes is sufficient to provide stabilization of the first and second statistical moments of the turbulence data (Nikora and Goring, 2000; Fox, 2002; Buffin-Bélanger and Roy, 2005). While the low order moments may stabilize, such a short duration does not allow K_m to converge. One minute time series will only capture thirty to sixty repetitions of macroturbulence cycles that pass the velocimetry instrument, and such low numbers lead to over-predicting K_m by 300%. We used the long time series results to formulate a time scale for minimum measurement length of turbulence data when information about macroturbulence is sought after. We symbolize the time scale as T_{min}. We derive T_{min} by considering the scaling of the macroturbulence

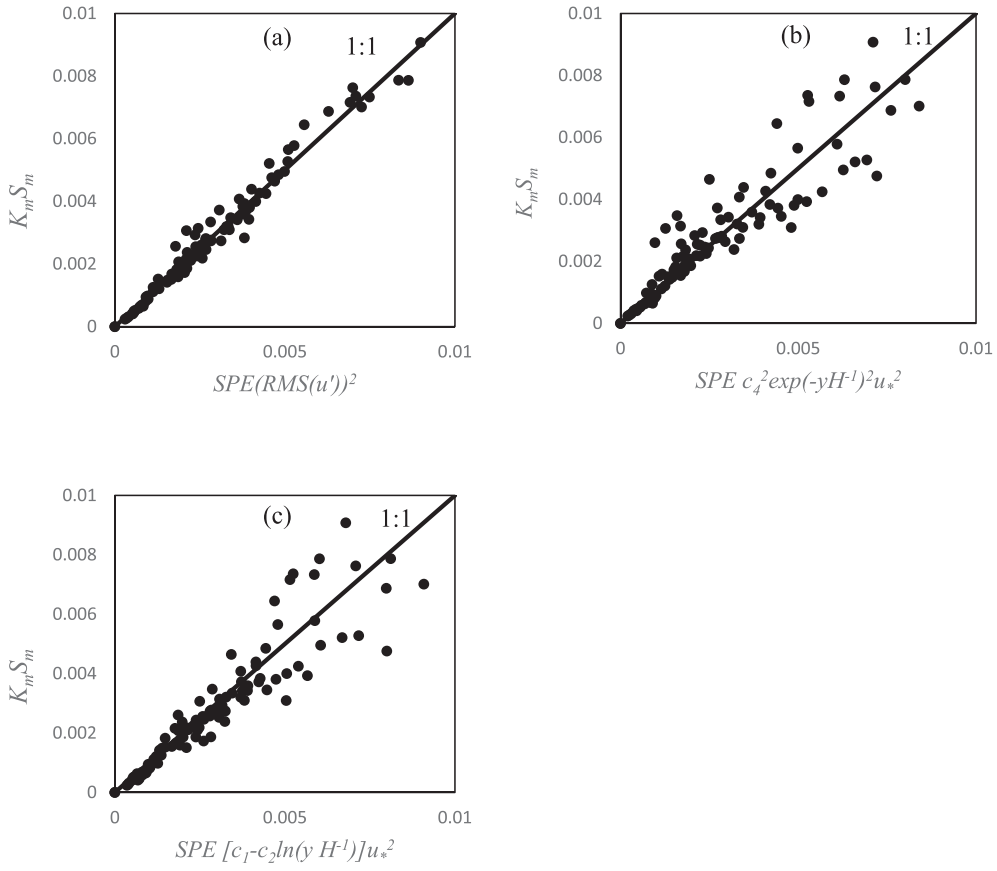

Fig. 11. Comparison of macroturbulence energy measured (y-axis) with the predictive equations (x-axis).

wavenumber in Fig. 8 ($K_m = c_mH^{-1}$ where $c_m = 0.48$), the sensitivity results for the long time series needed, and by invoking Taylor's hypothesis in which macroturbulence advects in the streamwise direction. The time scale for the minimum measurement length for macroturbulence is formulated as

$$T_{min} = N_{m-\,min}\, K_m^{-1}\, U^{-1} \tag{28}$$

where N_{m-min} is the minimum number of repetitions (i.e., cycles) of macroturbulence passing the velocimetry probe; and U and K_m are the streamwise velocity and macroturbulence wavenumber defined previously. We update Eq. (28) by substituting c_mH^{-1} instead of K_m as

$$T_{min} = N_{m-\,min}\, c_m^{-1}\, H\, U^{-1}. \tag{29}$$

We can parameterize N_{m-min} and c_m in Eq. (29) by considering the results of this study as well as citing the literature review in Roy et al. (2004). As mentioned, we found c_m to equal 0.48, which was nearly identical to the average value found for the studies reviewed in Table 1 of Roy et al. (2004). N_{m-min} is specified using data results in Fig. 7a. Results showed 17 min of measurements were needed when the wavenumber and streamwise velocity measured 3.75 m^{-1} and 0.94 m s^{-1}, respectively. N_{m-min} is calculated equal to 3600 repetitions, and Eq. (29) is updated as

$$T_{min} = \left(7.5 \times 10^3\right) H\, U^{-1}. \tag{30}$$

The time scale for measurement length (T_{min}) provides an approach to consider when information about macroturbulence is sought after. We remind the reader the numeric value in Eq. (30) is empirical and found from the sensitivity herein. Nevertheless future studies might consider this approach, and we especially highlight the significance of the result because Eq. (30) provides a time scale for measurement that is one and one-half orders of magnitude greater than measurement length considerations in previous turbulence studies in gravel bed rivers.

6. Conclusions

- Macroturbulence and bursting wavenumbers were constant in the outer region when scaled with the outer variable (i.e., the flow depth) for flow experiments over a gravel bed. The macroturbulence length scale found herein was nearly identical to the cross-study average reported in previous literature, which lent confidence to these results. One significant finding of this study is that the length scales were independent of distance above the boundary, aspect ratio, energy gradient, Froude number, or Shield's parameter.
- Data results from this study show that macroturbulence energy scales with the streamwise turbulence kinetic energy. The data scaling results are in agreement with the theoretical derivation shown herein of the macroturbulence energy scaling (see Eq. (17)) where we invoked: the spectral definition of the turbulence kinetic energy; the constant turbulence energy of the −1 spectral power region; and the order of magnitude difference between the bursting and macroturbulence wavenumbers. The energy finding in this paper is significant because an appropriate model-equation for turbulence kinetic energy can then be used to scale macroturbulence energy. We illustrate this point by scaling macroturbulence energy with two semi-empirical model-equations for turbulence kinetic energy commonly applied in turbulence studies, including logarithmic and exponential functions.
- A novel approach for predicting the macroturbulence period (Eq. (23)) is presented for the first time, to our knowledge, and the transferability is discussed. The macroturbulence period is defined with

outer variables, and the bounds on the coefficient are fitted to the experimental dataset reported herein. Coefficients in the macroturbulence period equation are an order of magnitude greater than the bursting period equation. Transferability of the equation for macroturbulence period is supported by the results' consistency with past macroturbulence studies, consistency with bursting formula, and consistency with flow visualization studies.

- A novel approach is also presented to predict the energy of macroturbulence. Direct use of the streamwise turbulence kinetic energy and indirect approximation via exponential and logarithmic functions all show potential for predicting macroturbulence energy. Transferability of the general form for the macroturbulence energy approach is supported by the derivation in Eq. (17) and fitting of the exponential and logarithmic equations by others. The transferability of the equation's exponential or logarithmic function will require some justification for a given application, at this time, given the semi-theoretical nature of the model-equations. Also, this was the first time the contribution of macroturbulence energy to overall turbulence energy was presented, so this parameter needs further investigation study. The energy finding in this paper shows usefulness for sediment transport applications, including prediction of the sediment carrying capacity via macroturbulence formula as one application to help close the gap between turbulence and fluvial sediment transport.
- Sensitivity analysis results from this paper showed that the macroturbulence wavenumber required a relatively long duration of data to stabilize. Results were used to formulate a time scale for minimum measurement length of turbulence data when information about macroturbulence is sought after, which is another contribution of the paper. The long measurement length needed for macroturbulence is significance because the time scale is one and one-half orders of magnitude greater than measurement length considerations in previous turbulence studies. Future work can consider the time scale when designing macroturbulence experiments.

Supplementary data to this article can be found online at https://doi.org/10.1016/j.geomorph.2019.02.006.

References

Albayrak, I., 2008. An Experimental Study of Coherent Structures, Secondary Currents and Surface Boils and Their Interrelation in Open-Channel Flow. Ph.D. thesis. Ecole Polytechnique Federale de Lausanne (EPFL), Switzerland.

Bagherimiyab, F., Lemmin, U., 2018. Large-scale coherent flow structures in rough-bed open-channel flow observed in fluctuations of three-dimensional velocity, skin friction and bed pressure. J. Hydraul. Res. 56 (6), 806–824. https://doi.org/10.1080/00221686.2017.1416686.

Belcher, B.J., 2009. Vortex Model of Open Channel Flows With Gravel Beds. Electronic Dissertation. University of Kentucky, Lexington, KY.

Belcher, B.J., Fox, J.F., 2009. Laboratory measurements of 3-D flow patterns and turbulence in straight open channel with rough bed. J. Hydraul. Res. 47 (5), 685–688. https://doi.org/10.1080/00221686.2009.9522050.

Belcher, B.J., Fox, J.F., 2011. Outer scaling for open channel flow over a gravel bed. J. Eng. Mech. 137 (1), 40–46. https://doi.org/10.1061/(ASCE)EM.1943-7889.0000200.

Boppe, R.S., Neu, W.L., 1995. Quasi-coherent structures in the marine atmospheric surface layer. J. Geophys. Res. Oceans 100 (C10), 20635–20648. https://doi.org/10.1029/95JC02305.

Buffin-Bélanger, T., Roy, A.G., 2005. 1 min in the life of a river: selecting the optimal record length for the measurement of turbulence in fluvial boundary layers. Geomorphology 68 (1), 77–94. https://doi.org/10.1016/j.geomorph.2004.09.032.

Calaf, M., Hultmark, M., Oldroyd, H.J., Simeonov, V., Parlange, M.B., 2013. Coherent structures and the k^{-1} spectral behaviour. Phys. Fluids 25 (12), 125107. https://doi.org/10.1063/1.4834436.

Cea, L., Puertas, J., Pena, L., 2007. Velocity measurements on highly turbulent free surface flow using ADV. Exp. Fluids 42 (3), 333–348. https://doi.org/10.1007/s00348-006-0237-3.

Clauser, F.H., 1954. Turbulent boundary layer in adverse pressure gradient. J. Aeronaut. Sci. 21, 91–108.

Clauser, F.H., 1956. The turbulent boundary layer. Adv. Appl. Mech. 4, 1–51.

Demare, S., Labraga, L., Tournier, C., 1999. Comparison and scaling of the bursting period in rough and smooth walls channel flows. J. Fluids Eng. 121 (4), 735–746. https://doi.org/10.1115/1.2823531.

Eder, F., De Roo, F., Rotenberg, E., Yakir, D., Schmid, H.P., Mauder, M., 2015. Secondary circulations at a solitary forest surrounded by semi-arid shrubland and their impact on eddy-covariance measurements. Agric. For. Meteorol. 211, 115–127. https://doi.org/10.1016/j.agrformet.2015.06.001.

Fox, J.F., 2002. Investigation of Flow Characteristics Around Submerged WSDOT Barbs. M. Sc. Thesis. Washington State University, Pullman, Washington.

Fox, J.F., Papanicolaou, A.N., Kjos, L., 2005. Eddy taxonomy methodology around a submerged barb obstacle within a fixed rough bed. J. Eng. Mech. 131 (10), 1082–1101. https://doi.org/10.1061/(ASCE)0733-9399(2005)131:10(1082).

George, W.K., Castillo, L., 1997. Zero-pressure-gradient turbulent boundary layer. Appl. Mech. Rev. 50 (12), 689–729. https://doi.org/10.1115/1.3101858.

Ghasemi, A., 2016. Study of Macroturbulence and Bursting via the −1 Spectral Power Law Region of Turbulent Open Channel Flow Over Gravel Beds. M.Sc. Thesis. University of Kentucky, Lexington, Kentucky.

Goring, D.G., Nikora, V.I., 2002. Despiking acoustic Doppler velocimeter data. J. Hydraul. Eng. 128 (1), 117–126. https://doi.org/10.1061/(ASCE)0733-9429(2002)128:1(117).

Guala, M., Hommema, S.E., Adrian, R.J., 2006. Large-scale and very-large-scale motions in turbulent pipe flow. J. Fluid Mech. 554, 521–542. https://doi.org/10.1017/S0022112006008871.

Guala, M., Metzger, M., McKeon, B.J., 2011. Interactions within the turbulent boundary layer at high Reynolds number. J. Fluid Mech. 666, 573–604. https://doi.org/10.1017/S0022112010004544.

Gulliver, J.S., Halverson, M.J., 1987. Measurements of large streamwise vortices in an open-channel flow. Water Resour. Res. 23 (1), 115–123. https://doi.org/10.1029/WR023i001p00115.

Hardy, R.J., Best, J.L., Parsons, D.R., Marjoribanks, T.I., 2016. On the evolution and form of coherent flow structures over a gravel bed: Insights from whole flow field visualization and measurement. J. Geophys. Res. Earth Surf. 121 (8), 1472–1493. https://doi.org/10.1002/2015JF003753.

Horoshenkov, K.V., Nichols, A., Tait, S.J., Maximov, G.A., 2013. The pattern of surface waves in a shallow free surface flow. J. Geophys. Res. Earth Surf. 118 (3), 1864–1876. https://doi.org/10.1002/jgrf.20117.

Hsu, C.C., Lee, W.J., Chang, C.H., 1998. Subcritical open-channel junction flow. J. Hydraul. Eng. 124 (8), 847–855. https://doi.org/10.1061/(ASCE)0733-9429(1998)124:8(847).

Hurther, D., Lemmin, U., Terray, E.A., 2007. Turbulent transport in the outer region of rough-wall open-channel flows: the contribution of large coherent shear stress structures (LC3S). J. Fluid Mech. 574, 465–493. https://doi.org/10.1017/S0022112006004216.

Hutchins, N., Marusic, I., 2007. Large-scale influences in near-wall turbulence. Philos. Trans. R. Soc. London, Ser. A 365 (1852), 647–664. https://doi.org/10.1098/rsta.2006.1942.

Katul, G., Chu, C.R., 1998. A theoretical and experimental investigation of energy-containing scales in the dynamic sublayer of boundary-layer flows. Bound.-Layer Meteorol. 86 (2), 279–312.

Kim, K.C., Adrian, R.J., 1999. Very large-scale motion in the outer layer. Phys. Fluids 11 (2), 417–422. https://doi.org/10.1063/1.869889.

Kironoto, B.A., Graf, W.H., Song, T., Lemmin, U., 1994. Turbulence characteristics in rough uniform open-channel flow. Proc. Inst. Civ. Eng. Water Marit. Energy 106 (4), 333–344.

Ling, C.H., 1995. Criteria for incipient motion of spherical sediment particles. J. Hydraul. Eng. 121 (6), 472–478.

Luchik, T.S., Tiederman, W.G., 1987. Timescale and structure of ejections and bursts in turbulent channel flows. J. Fluid Mech. 174, 529–552. https://doi.org/10.1017/S0022112087000235.

MacMahan, J., Reniers, A., Ashley, W., Thornton, E., 2012. Frequency–wavenumber velocity spectra, Taylor's hypothesis, and length scales in a natural gravel bed river. Water Resour. Res. 48 (9), W09548. https://doi.org/10.1029/2011WR011709.

MacVicar, B., Dilling, S., Lacey, J., 2014. Multi-instrument turbulence toolbox (MITT): Open-source MATLAB algorithms for the analysis of high-frequency flow velocity time series datasets. Comput. Geosci. 73, 88–98. https://doi.org/10.1016/j.cageo.2014.09.002.

Marquis, G.A., Roy, A.G., 2006. Effect of flow depth and velocity on the scales of macroturbulent structures in gravel-bed rivers. Geophys. Res. Lett. 33 (24), L24406. https://doi.org/10.1029/2006GL028420.

Matthes, G.H., 1947. Macroturbulence in natural stream flow. EOS Trans. Am. Geophys. Union 28 (2), 255–265. https://doi.org/10.1029/TR028i002p00255.

Monty, J.P., Hutchins, N., Ng, H.C.H., Marusic, I., Chong, M.S., 2009. A comparison of turbulent pipe, channel and boundary layer flows. J. Fluid Mech. 632, 431–442. https://doi.org/10.1017/S0022112009007423.

Nezu, I., 2005. Open-channel flow turbulence and its research prospect in the 21st century. J. Hydraul. Eng. 131 (4), 229–246. https://doi.org/10.1061/(ASCE)0733-9429(2005)131:4(229).

Nezu, I., Nakagawa, H., 1993. Turbulence in Open Channels. A. A. Balkema, Rotterdam, The Netherlands.

Nikora, V., 1999. Origin of the "−1" spectral law in wall-bounded turbulence. Phys. Rev. Lett. 83 (4), 734–737. https://doi.org/10.1103/PhysRevLett.83.734.

Nikora, V., 2005. Flow turbulence over mobile gravel-bed: spectral scaling and coherent structures. Acta Geophys. Pol. 53 (4), 539–552.

Nikora, V., Goring, D., 2000. Flow turbulence over fixed and weakly mobile gravel beds. J. Hydraul. Eng. 126 (9), 679–690. https://doi.org/10.1061/(ASCE)0733-9429(2000)126:9(679).

Nikora, V., Roy, A.G., 2012. Secondary flows in rivers: theoretical framework, recent advances, and current challenges. In: Church, M., Biron, P., Roy, A.G. (Eds.), Gravel-bed rivers: Processes, Tools, Environments. Wiley, Oxford, pp. 3–22.

Nikora, V., Goring, D., McEwan, I., Griffiths, G., 2001. Spatially averaged open-channel flow over rough bed. J. Hydraul. Eng. 127 (2), 123–133. https://doi.org/10.1061/(ASCE)0733-9429(2001)127:2(123).

Perry, A.E., Abell, C.J., 1975. Scaling laws for pipe-flow turbulence. J. Fluid Mech. 67 (02), 257–271. https://doi.org/10.1017/S0022112075000298.

Perry, A.E., Chong, M.S., 1982. On the mechanism of wall turbulence. J. Fluid Mech. 119, 173–217. https://doi.org/10.1017/S0022112082001311.

Perry, A.E., Henbest, S., Chong, M.S., 1986. A theoretical and experimental study of wall turbulence. J. Fluid Mech. 165, 163–199. https://doi.org/10.1017/S002211208600304X.

Rodríguez, J.F., García, M.H., 2008. Laboratory measurements of 3-D flow patterns and turbulence in straight open channel with rough bed. J. Hydraul. Res. 46 (4), 454–465. https://doi.org/10.3826/jhr.2008.2994.

Roy, A.G., Buffin-Belanger, T., Lamarre, H., Kirkbride, A.D., 2004. Size, shape and dynamics of large-scale turbulent flow structures in a gravel-bed river. J. Fluid Mech. 500, 1–27. https://doi.org/10.1017/S0022112003006396.

Shvidchenko, A.B., Pender, G., 2001. Macroturbulent structure of open-channel flow over gravel beds. Water Resour. Res. 37 (3), 709–719. https://doi.org/10.1029/2000WR900280.

Stewart, R.L., Fox, J.F., 2015. Role of macroturbulence to sustain turbulent energy in decelerating flows over a gravel bed. Geomorphology 248, 147–160. https://doi.org/10.1016/j.geomorph.2015.07.028.

Tchen, C.M., 1953. On the spectrum of energy in turbulent shear flow. J. Res. Natl. Bur. Stand. 50, 51–62. https://doi.org/10.6028/jres.050.009.

Townsend, A.A., 1976. The Structure of Turbulent Shear Flow. 2nd edn. Cambridge University Press, pp. 150–158.

Tritico, H.M., Hotchkiss, R.H., 2005. Unobstructed and obstructed turbulent flow in gravel bed rivers. J. Hydraul. Eng. 131 (8), 635–645. https://doi.org/10.1061/(ASCE)0733-9429(2005)131:8(635).

Venditti, J.G., Bennett, S.J., 2000. Spectral analysis of turbulent flow and suspended sediment transport over fixed dunes. J. Geophys. Res. Oceans 105 (C9), 22035–22047. https://doi.org/10.1029/2000JC900094.